PCCP

RSCPublishing

PAPER

View Article Online
View Journal | View Issue

Published on 31 January 2013. Downloaded by University of Colorado at Boulder on 10/01/2014 19:38:12.

Cite this: *Phys. Chem. Chem. Phys.*, 2013, **15**, 10616

Multiphoton photoelectron emission microscopy of single Au nanorods: combined experimental and theoretical study of rod morphology and dielectric environment on localized surface plasmon resonances†

Andrej Grubisic, Volker Schweikhard, Thomas A. Baker and David J. Nesbitt*

Received 6th December 2012,
Accepted 28th January 2013

DOI: 10.1039/c3cp44385j

www.rsc.org/pccp

Multiphoton photoelectron emission from individual Au nanorods deposited on indium tin oxide (ITO) substrates is studied *via* scanning photoionization microscopy, based on femtosecond laser excitation at frequencies near the rod longitudinal surface plasmon resonance (LSPR). The observed resonances in photoemission correlate strongly with plasmon resonances measured in dark field microscopy (DFM), thus establishing a novel scheme for wavelength-resolved study of plasmons in isolated metallic nanoparticles based on highly sensitive electron counting methods. In this work, we explore experimental and theoretical effects of (i) morphology and (ii) aspect ratio (AR) for longitudinal plasmon resonance behavior in Au nanorods. A quasilinear dependence between LSPR and aspect ratio (AR) is experimentally determined [$\Delta\lambda \approx +100(10)$ nm/AR unit] for Au nanorods on ITO, in excellent agreement with the first principles value from finite element computer modeling [$\Delta\lambda = +108(5)$ nm/AR unit]. Interestingly, however, LSPR values for larger *vs.* smaller diameter rods ($w \approx 20$ nm and 10 nm) are systematically red-shifted [$\Delta E \approx -0.03(1)$ eV; $\Delta\lambda \approx +15(5)$ nm at $\lambda \approx 800$ nm], indicating that electromagnetic retardation effects must also be considered for highest accuracy in LSPR position. To augment these results, the influence of the dielectric environment on the rod LSPR has been explored both experimentally and numerically. In particular, detailed finite-element simulations for ITO supported Au nanorods are found to yield plasmon resonances in near quantitative agreement ($\Delta E \approx \pm 0.04$ eV) with experiment, with residual differences arising from uncertainty in the refractive index of the ITO thin film. Furthermore, the results indicate that plasmon resonance predictions based on infinitely thick ITO substrates are reliable to a few meV for film thicknesses larger than approximately twice the rod width.

I. Introduction

Coherent oscillation of conduction electrons can be induced by the incident electromagnetic radiation if the frequency matches the intrinsic plasma frequency of the metal.[1] For most metals, this occurs deep in the ultraviolet (UV) region, but for coinage metals, *e.g.*, Cu and Au, it takes place closer to the visible spectral range. In conjunction with the spatial boundary conditions in metallic nanoparticles, this gives rise to a localized surface plasmon resonance (SPR), which manifests itself by greatly enhanced light scattering and/or intense absorption at specific frequencies. These plasmons are extremely sensitive to particle size, shape and the dielectric environment, thus providing a handle for "tuning" the optical response of nanostructures throughout the visible (VIS) and the near-infrared (NIR) spectral range. As a result, nanoparticles are promising for a plethora of applications, ranging from light absorption enhancers in solar cells,[2–5] subdiffraction-limited light guides in plasmonic devices,[6–8] photothermal anti-cancer agents in medicine,[9–11] ultrasensitive chemical detectors[12–19] and even THz generators,[20] to name only a few.

Of the various nanoparticle morphologies,[21–31] Au nanorods have received particular attention due to their favorable optical response, small size, chemical inertness and biocompatibility. Their asymmetric shape supports two types of plasmons: (i) a *longitudinal* surface plasmon (LSPR), where the conduction electrons oscillate in the long axis direction (b), and (ii) two degenerate *transverse* plasmons modes, each aligned along the

---

JILA, University of Colorado and National Institute of Standards and Technology, and Department of Chemistry and Biochemistry, University of Colorado, Boulder, Colorado 80309-0440, USA. E-mail: djn@jila.colorado.edu; Fax: +1 303 735-1424; Tel: +1 303 492-8857

† Electronic supplementary information (ESI) available. See DOI: 10.1039/c3cp44385j

This journal is © the Owner Societies 2013

Published on 31 January 2013. Downloaded by University of Colorado at Boulder on 10/01/2014 19:38:12.

minor axes (a). In the so-called electrostatic limit (*i.e.*, both axes a, $b \ll \lambda$), these resonances are governed by a single geometric factor, the aspect ratio (b/a = AR), with the longitudinal (transverse) plasmon resonance shifting to the red (blue) with increasing AR, respectively.[32–41] While the transverse SPR moves only over a relatively narrow wavelength range ($\sim$20–30 nm), the longitudinal plasmon resonance can be tuned almost through the entire visible (VIS) and even into the infrared (IR) region by simply changing the rod AR. The broad tunability of longitudinal SPRs in Au nanorods has established these species as remarkably promising candidates for plasmonic applications, which has generated keen interest in how secondary factors, such as the overall rod size, influence plasmon resonance properties. Indeed, recent studies have suggested that electrostatic modeling inadequately describes the optical response for nanorod widths (w) in excess of $\sim$30 nm, thus requiring more sophisticated treatment dependent on explicit nanoparticle shape and dimensions.[42–47] In support of this, the results reported herein demonstrate that near quantitative level ($\Delta E = \pm 0.04$ eV) predictions of plasmon resonance frequencies ($\Delta\lambda = \pm 20$ nm at λ = 800 nm) may not be feasible with electrostatic treatments for widths larger than $w \sim 15$ nm and lengths $l \sim 50$ nm.

Another relevant factor influencing the LSPR is the dielectric environment. The influence of isotropic media on plasmons has been studied extensively, with results clearly establishing a systematic red-shift in the plasmon resonance with increasing refractive index of the medium.[38,41,48–51] While this general trend holds universally, it is far less obvious how to think about finite and/or discontinuous environments such as, for example, experienced by particles on a substrate. Since the majority of applications envision using such supported nanoparticles, it is critical to understand how asymmetric environments affect plasmon resonances.[52–54] Analytical solutions are known for some specific cylindrically symmetric arrangements, *e.g.*, spheres[55] and coated spheres[56] on a substrate as well as oblate/prolate ellipsoids with unique axis pointing normal to the substrate surface.[57] Unfortunately however, none of these apply in the most ubiquitous scenario of nanorods lying parallel to the surface, making numerical calculations the only rigorous approach for studying arbitrary particle shapes in asymmetric dielectric environments.

The complexity of such calculations has fostered the use of approximate models for the asymmetric environment, where a uniform medium is assumed with an average index of refraction given by:

$$n_{\text{eff}} = \alpha n_1 + (1 - \alpha) n_2 \tag{1}$$

In this expression, n_1 and n_2 are the refractive indices for "superstrate" and substrate, respectively, and α is an empirical constant ($0 < \alpha < 1$) that reflects particle sensitivity to the two media.[58–61] However, without extensive benchmarking of experimental *vs.* predicted behavior for well characterized nanoparticle systems and dielectric environments, the accuracy of these and other such approximations is hard to predict *a priori*. Indeed, it is toward a better understanding of the structural, environmental and material influence on plasmonic particle response in asymmetric environments that the present studies are specifically directed.

In particular, the work focuses on thin film indium tin oxide (ITO), due to its ubiquity in many existing applications requiring optically (VIS/NIR) transparent, conductive substrates. It mainly comes in the form of thin, annealed films whose index of refraction varies with method of preparation and therefore necessarily has to be determined experimentally. As we shall demonstrate, classical electrodynamics calculations as employed in COMSOL yield results in near quantitative (*i.e.*, $\Delta E = \pm 0.04$ eV) agreement with experimental observation, limited only by residual experimental uncertainty in the particle dielectric environment. Additionally, for plasmon resonance predictions at such accuracy, we show that the finite ITO thickness (d_f) must also be taken into account, with correct convergence to infinite slab predictions achieved only for $d_f \geq 2w$.

To establish such benchmarks, we employ a powerful combination of (i) scanning photoionization microscopy (SPIM), (ii) dark field microscopy (DFM), and (iii) secondary electron microscopy (SEM) to experimentally correlate near- (SPIM) and far-field (DFM) plasmonic response of individual Au nanorods with their structure (SEM). While near- and far-field signatures of localized surface plasmons may generally differ,[62–65] they spectrally coincide in the case of the longitudinal SPR in Au nanorods.[66] As a result, the greater detection sensitivity of SPIM can be successfully employed to infer the longitudinal plasmon resonances in Au nanorods that may be too small to study with DFM alone. When combined with detailed electrodynamics calculations, these correlated microscopy techniques lay a foundation for predictive characterization of environmental and size dependent effects on plasmon resonance behavior, which represents the main thrust of the present work.

II. Experimental methods

IIA. Sample preparation and characterization

Commercially available (Nanorodz™; Nanopartz, Inc.) aqueous solutions of Au nanorods (NR) of two different sizes are used for the present studies (Nanopartz P/N: 30-10-850 and 30-25-750). A dimensional analysis of the two samples (see Fig. 1) yields the following ensemble averaged values for rod dimensions and aspect ratios (AR) with standard deviations reported in parentheses: (i) Sample 1 (N = 204): $\langle l \rangle$ = 39(6) nm, $\langle w \rangle$ = 10(2) nm, $\langle \text{AR} \rangle$ = 3.9(7); (ii) Sample 2 (N = 385): $\langle l \rangle$ = 63(5) nm, $\langle w \rangle$ = 20(2) nm, $\langle \text{AR} \rangle$ = 3.2(3). UV-VIS spectrum (see Fig. 1) of the stock solution of the smaller Au nanorods (Sample 1) exhibits a strong longitudinal plasmon resonance at $\langle \lambda_{\text{Pl}} \rangle_{\text{L}}^{\text{H}_2\text{O}} = 820(2)$ nm with a 1σ width, $\sigma_{\text{L}}^{\text{H}_2\text{O}} = 60(5)$ nm, and a weaker transverse plasmon resonance at $\langle \lambda_{\text{Pl}} \rangle_{\text{T}}^{\text{H}_2\text{O}} = 510(1)$ nm and a width $\sigma_{\text{T}}^{\text{H}_2\text{O}} = 13(1)$ nm. For the larger Au nanorods (Sample 2), the peaks are observed at $\langle \lambda_{\text{Pl}} \rangle_{\text{L}}^{\text{H}_2\text{O}} = 725(2)$ nm and $\langle \lambda_{\text{Pl}} \rangle_{\text{T}}^{\text{H}_2\text{O}} = 512(1)$ nm with the corresponding 1σ widths $\sigma_{\text{L}}^{\text{H}_2\text{O}} = 35(3)$ nm and $\sigma_{\text{T}}^{\text{H}_2\text{O}} = 14(1)$ nm, respectively.

Published on 31 January 2013. Downloaded by University of Colorado at Boulder on 10/01/2014 19:38:12.

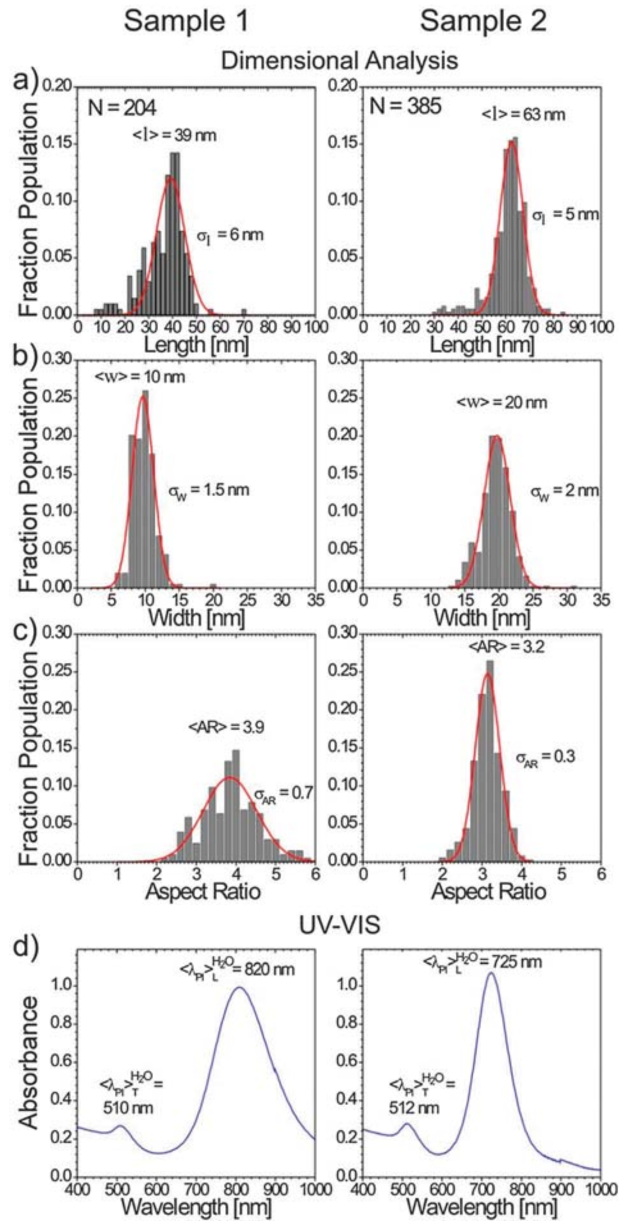

Fig. 1 SEM/TEM dimensional analysis of the two rod samples (left: Sample 1; right: Sample 2): (a) Rod length (*l*); (b) rod width (*w*); (c) rod aspect ratio (AR); (d) UV-VIS spectra of the aqueous stock solutions of the two rod samples.

To prepare the samples, 40 μl of stock aqueous solution of Au nanorods are spin-cast onto a rotating (1500 rpm) ITO-coated glass coverslip (Thin Film Devices, Inc.), patterned to allow particle registration as reported previously.[66] Immediately prior to sample deposition, the coverslips are ozone cleaned for 5 minutes to remove organic contaminants from the coverslip surface, which greatly improves surface wetting and consequently leads to more uniform nanoparticle coverage. The sample is then sequentially rinsed with deionized water, methanol and acetone to remove any non-colloidal solute [*e.g.*, cetyl-trimethyl-ammonium-bromide (CTAB)] added to stabilize nanoparticle solutions. Under these preparation conditions, coverages of 0.1 NR/μm^2 are typically obtained.

Variable Angle Spectroscopic Ellipsometry (VASE®; J. A. Woollam Co., Inc) is utilized to experimentally determine the thickness and dispersion relation for the ITO films. In this technique, the intensity and polarization of reflected light from the substrate is measured as a function of wavelength λ and incident angle (θ_i), yielding ellipsometric parameters $\Psi(\lambda, \theta_i)$, and $\Delta(\lambda, \theta_i)$. These experimental parameters (see ESI†) are then fit based on a model for the substrate refractive index and structure, allowing very precise determination of film thickness and index of refraction. For further details on the technique, the reader is referred to ref. 67.

To describe the substrates in the present study, ellipsometric model is used that assumes a flat ITO film of thickness d_f on top of a flat glass slab of sufficient thickness for the reflection from the back surface to be safely neglected. Both glass and ITO are presumed to be non-absorbing materials (n is real) with the refractive index described by the Cauchy dispersion equation $n = A + B/\lambda^2$ in the studied wavelength range. Measurements were performed on three different coverslips from the same batch in order to determine mean values and sample-to-sample variation. The ITO films, nominally 10 nm by manufacturer quote, are in fact ellipsometrically determined to be 18(1) nm, and are well modelled by the following Cauchy dispersion relation in the wavelength range of interest, *i.e.*, 400–1000 nm:

$$n(\lambda) = 1.917 + 0.045/\lambda[\mu\mathrm{m}]^2 \qquad (2)$$

Though some variability between the samples is observed, the measured index of refraction in all cases falls within ±0.01 RIU (refractive index units) of the values predicted by eqn (2) and is in relatively good agreement with previous measurements on annealed ITO thin films.[68]

IIB. Scanning photoionization microscopy (SPIM)

The tunable fundamental output (λ = 710–890 nm; $E_{h\nu}$ = 1.75–1.40 eV) of an ultrafast Ti:Sapphire laser system is focused by a reflective-type microscope objective (numerical aperture, NA = 0.65) to a diffraction limited spot on an ITO-coated coverslip sample located in vacuum ($\sim 5 \times 10^{-7}$ Torr). At the focus, the high intensity laser beam promotes a fraction of the electrons within the sample material to the vacuum level, where they are accelerated and detected with a Channeltron electron multiplier located ~1 cm above the sample. For typical material work functions of the metal nanoparticles (Φ_{Au} = 4.6–5.1 eV,[69] Φ_{ITO} = 4.4–4.7 eV depending on crystal facet),[70] n = 3–4 photons with λ in the 700–900 nm range ($n > \Phi/E_{h\nu}$) are energetically required to photoemit a single electron. For a more detailed description of the technique and the experimental setup, the reader is referred to previous work.[71,72]

In the current study, Fourier-transform limited laser pulses ($\tau_P \sim$ 40 fs) at a repetition rate of 90 MHz are focused to a diffraction limited spot (full-width-half-maximum, FWHM = 0.515 × λ/NA = 634 nm for λ = 800 nm), yielding typical pulse energies attenuated down to E_P = 0.2 pJ and corresponding peak laser intensities of $I = 6 \times 10^8$ W cm^{-2}. At such laser intensities, multiphoton absorption leads to an intentionally small (10^{-4}) but still easily measurable probability of photoelectron

This journal is © the Owner Societies 2013

Published on 31 January 2013. Downloaded by University of Colorado at Boulder on 10/01/2014 19:38:12.

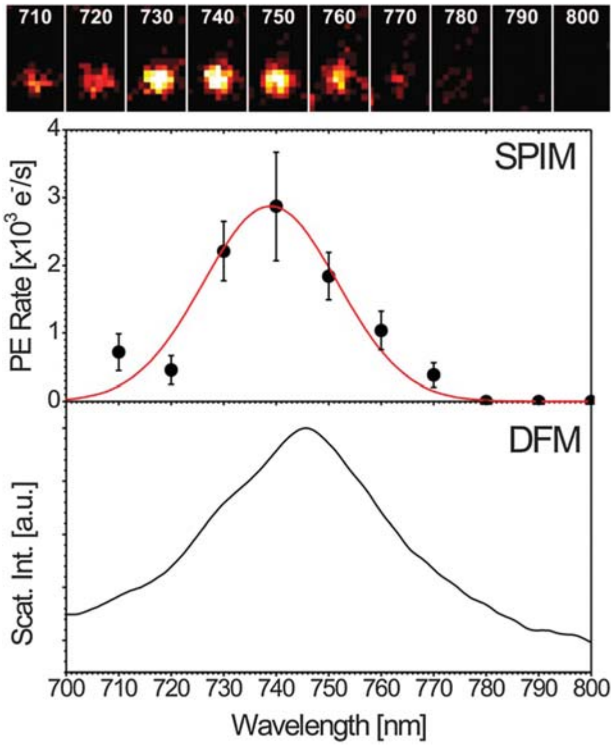

Fig. 2 Correspondence between the photoelectron emission and scattering spectra for the same Au nanorod (Sample 2). A sequence of SPIM images of the same nanorod on ITO shown at the top are recorded with circularly polarized laser excitation at the indicated center wavelength. Peak values of 2D Gaussian best-fit to the signal in these images are used to obtain photoelectron emission spectrum (solid circles). A gaussian fit to the datapoints is also shown. The dark-field scattering spectrum shown at the bottom reveals a clear correspondence between multiphoton photoemission (SPIM) and scattering (plasmon) (DFM) resonances.

emission per pulse, typically yielding photoemission rates up to 10^4 e^- per s from individual Au nanorods and essentially negligible background signal from the ITO thin film (<0.1 e^- per s) [Fig. 2 (top)]. In order to eliminate the known dependence of the photoemission signal on the direction of laser polarization, all data presented in this study are recorded with circularly polarized light.[66,73,74]

IIC. Dark-field microscopy (DFM)

Scattering spectra of individual Au nanorods on ITO-coated coverslips are measured with a dark-field microscope system (Olympus IX-71) coupled to a spectrometer (Acton SpectraPro 150, 150 g mm^{-1} diffraction grating) and an EMCCD camera (Princeton Instruments, Cascade II) operated without multiplication. Dark-field illumination is achieved by flooding a dark-field condenser (Olympus U-DCD, NA = 0.80–0.92) with unpolarized white light from a tungsten/halogen source. Scattered light from nanoparticles is collected by a 40× Plan Fluorite infinity-corrected air objective (Olympus UPLFLN40X, NA = 0.75). This arrangement strikes an optimal balance between scattered and background light, resulting in typical dark field signal-to-background ratio of S/B ∼ 15 for larger rods (Sample 2) in wide-field. Spectrally resolved signal from a particular particle is obtained by hardware binning a horizontal strip on the CCD chip whose width is approximately twice the imaged particle diameter, thus ensuring complete integration of the scattered light. Background is removed by subtracting signal from a horizontal strip of identical thickness containing no particles. To correct for spectral non-uniformity in the lightsource, the spectrum is acquired and subsequently divided into the background-subtracted signal, thus resulting in a single particle scattering spectrum. Detailed information on the experimental setup has been published elsewhere.[66]

Scattering spectra of many hundreds of Au nanorods are recorded immediately upon sample preparation as well as after the SPIM studies. No significant difference between spectra obtained before and after SPIM measurements is observed, therefore ruling out irreversible damage due to heating or electron-induced chemical modifications under typical SPIM laser illumination conditions. Dark field microscopy scattering studies have been performed only on the larger (Sample 2) Au rods, due to their substantially larger (16-fold) optical scattering cross-sections with respect to the smaller (Sample 1) Au nanorods.

IID. Secondary electron microscopy (SEM)

All SEM images are acquired on a FEI Nova NanoSEM 630 system using a through-lens detector (TLD) in immersion mode. For improved collection efficiency of secondary electrons, the front grid of the detector is biased to +150 V. Typically a 10 kV electron beam at a 1.5 spot size is employed, with signal generally integrated for 90 μs. At these conditions, a spatial resolution of ∼1–2 nm and a signal-to-noise ratio, S/N ∼ 20, for larger rods (Sample 2) is routinely achieved. The SEM studies of Au nanorod samples are always performed last to avoid irreversible effects of the fast electron beam on nanoparticles and their plasmonic properties.[75]

IIE. Theoretical methods

The near-field distribution of electric fields and far-field properties (*i.e.*, absorption, scattering and extinction spectra) of supported Au nanorods are numerically calculated with a commercial software package COMSOL (v4.2) that employs finite element method (FEM) analysis. A lozenge-like shape of nanorods is assumed in direct contact with a perfectly flat ITO film on top of an infinite slab of glass with the rod unique axis parallel to the substrate. Au is modelled with previously published bulk dielectric function,[76] whereas ITO is assumed to be a non-absorbing material in the wavelength range studied, with the dielectric constant derived from the experimentally measured dispersion eqn (2). The ITO film thickness in the calculation is set to the experimentally observed value of d_f = 18 nm. For the glass substrate, a BK7 refractive index $n = 1.5046 + 0.0042/\lambda[\mu m]^2$ is used.[77] Given the relative distance of the nanorod from the glass layer, the exact dispersion relation proves non-critical. Vacuum (n = 1) is assumed as the superstrate. To extract the longitudinal plasmon resonance frequencies, the calculated absorption spectra are fitted to a Lorentzian lineshape.

Published on 31 January 2013. Downloaded by University of Colorado at Boulder on 10/01/2014 19:38:12.

III. Results and analysis

Multiphoton photoelectron emission from Au nanorods has been previously shown to dramatically increase in the presence of a longitudinal plasmon resonance, due to the accompanying local electric near-field enhancement.[66] Since the square magnitude of this enhancement in the vicinity of the longitudinal SPR closely tracks the rod scattering (and absorption) cross-section, SPIM provides similar information as DFM in the case of Au NRs. For example, the peak resonances in the photoemission spectra correspond to those observed in the scattering spectra (see Fig. 2),[66] allowing either to be used to determine the position of the longitudinal plasmon resonance. This correlation is particularly valuable for studying smaller rods (w < 10 nm), whose scattering intensity becomes prohibitively weak to measure.

To explore the effect of nanoparticle structure on the longitudinal plasmon resonance, the influence of rod aspect ratio (AR) is investigated first. For ellipsoidal particles in the electrostatic limit, aspect ratio is the only structural parameter that can influence the position of the plasmon resonance.[35,38,78] In particular, increasing the rod aspect ratio red-shifts the longitudinal plasmon resonance, as qualitatively confirmed in Fig. 3 for a series of rods (Sample 2). The results on a substantially larger dataset are quantitatively depicted in Fig. 4 both for the smaller (Sample 1; N = 58) and larger rods (Sample 2; N = 72). The dramatic red-shift of the longitudinal plasmon resonance with increasing rod aspect ratio confirms that rod AR is indeed the dominant factor that influences the longitudinal plasmon resonance. The predictions for both rod sizes are also plotted in Fig. 4 (solid lines) and show excellent agreement with no adjustable parameters. For example, the LSPR sensitivity to aspect ratio [*i.e.*, +100(10) nm/AR] agrees quite well with COMSOL calculations, which predict +104 nm/AR and +113 nm/AR for w = 10 nm and w = 20 nm rods, respectively.[79] Even absolute values for the plasmon resonance positions agree with experimental results to ±20 nm throughout the monitored spectral range, with only slight deviations occuring at the shortest (∼700 nm) and longest (∼850 nm) wavelengths employed. This high level of agreement strongly indicates that the experimental environment is accurately modeled by calculations, with bulk refractive indices correctly describing the dielectric properties of all materials involved and negligible effects from ligand coverage on the rod surface.

If aspect ratio were the only structural parameter affecting the plasmon resonances (*i.e.*, the electrostatic limit), the two datasets in Fig. 4 should fall on the exact same trendline. However, the statistical quality of the data is already quite adequate to note that the larger rods appear slightly red-shifted with respect to the smaller rods. Thus the overall particle size clearly remains a weak but contributing factor, *i.e.*, indicating that non-electrostatic *retardation* effects become relevant as the rod width and length exceed ∼15 nm and ∼50 nm, respectively.[42–47,78] To further elucidate the effect of rod size, the longitudinal SPR frequency is plotted in Fig. 5 as a function of rod width at a fixed aspect ratio of AR = 4. The two experimental datapoints are obtained from linear least squares fits to the data in Fig. 4 (dashed lines). By way of comparison, Fig. 5 also shows calculated COMSOL LSPR values for rods with AR = 4 on a vacuum-ITO(18 nm)-glass interface as a function of rod width (solid line), which agree well with the experimental observations. Also worth noting, the residual upward curvature in these calculations clearly reveals non-vanishing sensitivity in the plasmon resonances to rod width well below 10 nm, with a putative ±0.04 eV (*i.e.*, ±20 nm at λ = 800 nm) accuracy in the electrostatically determined LSPR only achieved for w < 15 nm. Analogous nonlinear dependence of the LSPR position on rod width for a fixed rod aspect ratio has also been previously noted by Ni *et al.*[80] In Fig. 5, the predicted dependence of the longitudinal SPR based on an empirical model by Encina and Coronado is also shown (dashed line) and will be discussed later in greater detail.[42]

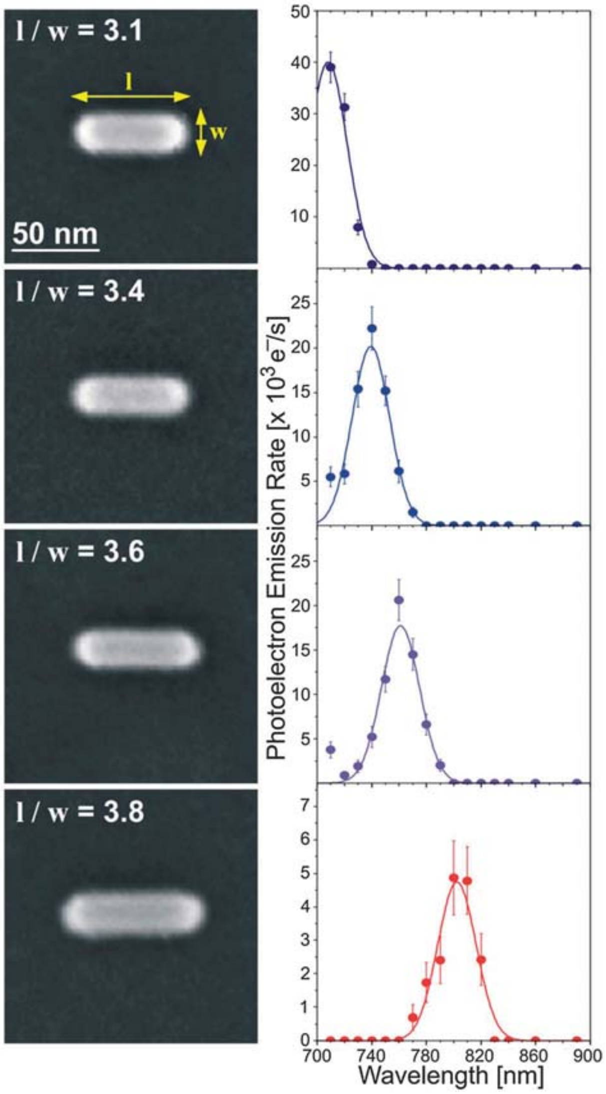

Fig. 3 SEM images and the corresponding photoemission spectra of a series of Au nanorods with increasing aspect ratio (AR = l/w = length/width). Increase in the rod aspect ratio results in a red-shifted longitudinal SPR.

A third factor that significantly influences the plasmon resonances is the particle dielectric environment. The calculated

View Article Online

Published on 31 January 2013. Downloaded by University of Colorado at Boulder on 10/01/2014 19:38:12.

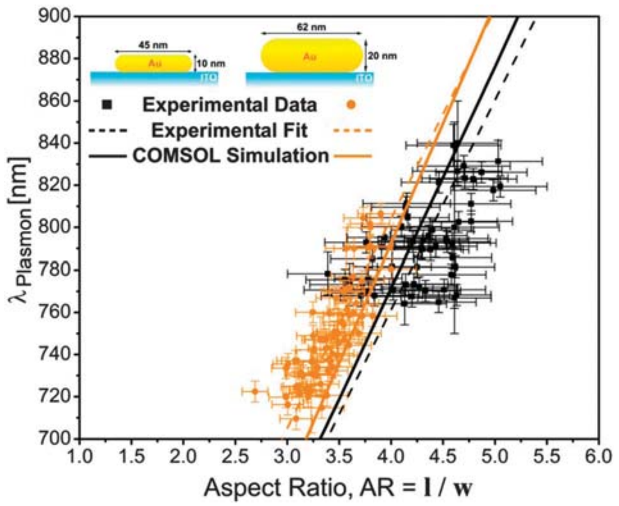

Fig. 4 Longitudinal SPR, $\lambda_{\mathrm{Plasmon}}$, as a function of rod aspect ratio for smaller [Sample 1 (squares): $\langle w \rangle$ = 10(2) nm] and larger rods [Sample 2 (circles): $\langle w \rangle$ = 20(2) nm]. Linear fits to the experimental data (dashed) and the predictions of numerical COMSOL simulations (solid) are shown as lines.

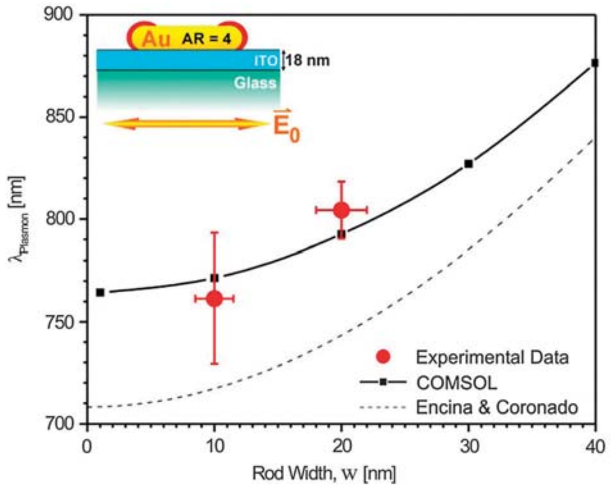

Fig. 5 Longitudinal SPR as a function of rod width (w) for a fixed rod aspect ratio (AR = 4). (circles) Experimental datapoints extracted from data in Fig. 4; (squares/solid line) COMSOL predictions for hemispherically capped Au cylinders on d_f = 18 nm thick ITO film; (dashed) semiempirical predictions for Au cylinders in a uniform medium with refractive index, n = 1.25, from ref. 42. The dependence of the plasmon resonance for these rod widths already indicates deviations from the small-particle electrostatic limit.

longitudinal SPR frequency as a function of the surrounding refractive index is shown in Fig. 6 for AR = 4 rods (with w = 10 nm and 20 nm) imbedded in a uniform dielectric surrounding. By comparison with the data in Fig. 5, one can extract an effective uniform refractive index for the ITO–glass–vacuum interface of n_{eff} = 1.25(5). Based on the measured ITO refractive index [see eqn (2)] in this wavelength range of n_{ITO} = 2.0, eqn (1) yields an approximate sensitivity factor of α = 0.75(5). This would suggest that the rod shape is substantially more sensitive to the superstrate (*i.e.*, vacuum) than to the ITO substrate, consistent with the fact that the majority of the rod surface is in contact with the vacuum rather than ITO.

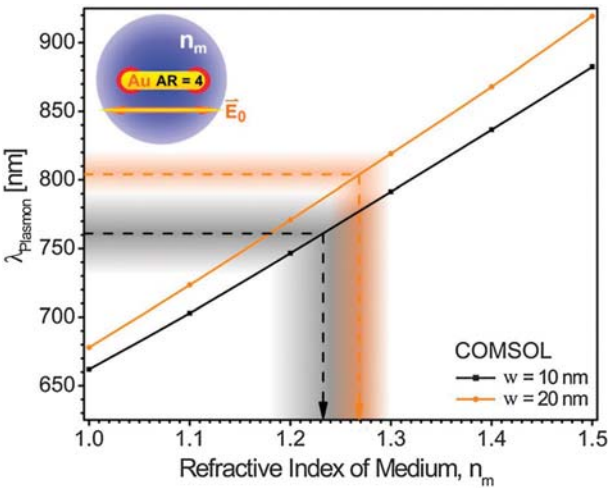

Fig. 6 Calculated longitudinal plasmon resonance, $\lambda_{\mathrm{Plasmon}}$, for hemispherically-capped Au cylinders (*i.e.*, lozenges) of two different sizes [(squares) w = 10 nm; (circles) w = 20 nm] and AR = 4 in a uniform medium with a refractive index n_{m}. Experimental datapoints from Fig. 5 are used to infer the effective refractive index of the Glass–ITO–Air environment n_{eff} = 1.25(5) (dashed lines; shading reflects the experimental error bars).

The effect of the surrounding on LSPR can be explored further by comparing ensemble data for Au nanorods on an ITO-coated coverslip [n_{eff} = 1.25(5)] and in aqueous solution (n_w = 1.33). Based on relative refractive indices of the surrounding media, the longitudinal SPR ought to slightly blue-shift upon transfer of rods from an aqueous environment onto an ITO-coated coverslip. The distribution of longitudinal plasmon resonances for the subpopulation of smaller nanorods (Sample 1, w = 10 nm) on ITO substrate measured by SPIM is shown in Fig. 7 (top), where the tuning range of our current Ti:Sapphire laser prevents the complete distribution from being measured. However, by counting the rods that exhibit tails increasing towards the blue end of the photoemission spectra or were not observed at all due to insufficiently large AR (as identified by SEM), one can approximately infer populations in the full normal distribution (solid line), for which the ensemble-averaged peak resonance of $\langle \lambda_{\mathrm{Pl}} \rangle_{\mathrm{L}}^{\mathrm{ITO}} = 765(5)$ nm and a 1σ width of $\sigma_{\mathrm{L}}^{\mathrm{ITO}} = 40(5)$ nm is obtained on the vacuum–ITO interface. By way of comparison, the ensemble-averaged LSPR distribution (see Fig. 7, bottom) determined from the UV-VIS spectrum for an aqueous solution of the same Au nanorod sample is red-shifted to $\langle \lambda_{\mathrm{Pl}} \rangle_{\mathrm{L}}^{\mathrm{H_2O}} = 820(2)$ nm, in good qualitative agreement with expectation.

To explore whether these observations are also in quantitative agreement, the measured distibutions are compared with COMSOL predictions based on the probability density distribution of rod aspect ratios, P(AR), experimentally obtained from dimensional analysis of Au nanorod samples (see Fig. 1). If AR is assumed to be the only structural factor influencing the longitudinal SPR, the probability density distribution of plasmon resonances $P(\lambda_{\mathrm{Pl}})$ for a given rod sample can be predicted from the simple differential Jacobian relation:

$$P(\lambda_{\mathrm{Pl}}) = P(\mathrm{AR})\left\{\frac{\mathrm{dAR}}{\mathrm{d}\lambda_{\mathrm{Pl}}}\right\} \tag{3}$$

Published on 31 January 2013. Downloaded by University of Colorado at Boulder on 10/01/2014 19:38:12.

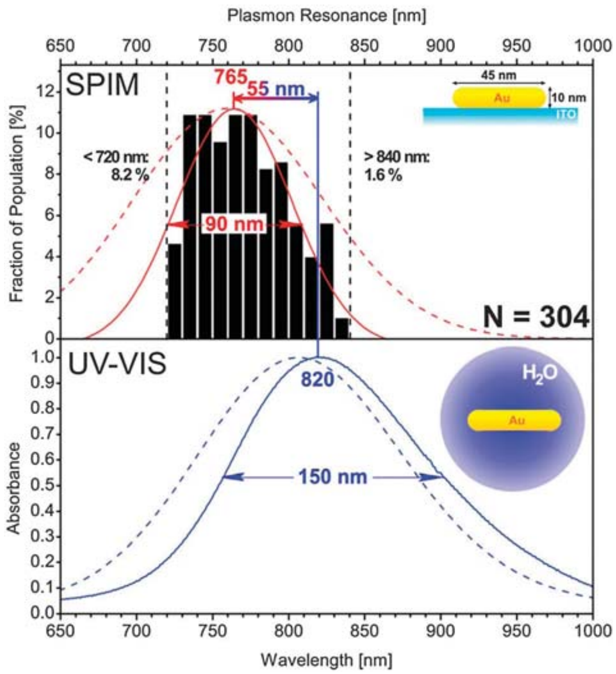

Fig. 7 Distribution of plasmon resonances for Au nanorods [Sample 1: $\langle l \rangle$ = 39(6) nm, $\langle w \rangle$ = 10(2) nm] on ITO (top) and in water (bottom) measured in SPIM and UV-VIS spectrophotometer, respectively. Gaussian best-fit line (solid line) is overlayed on the distribution inferred from SPIM. A substantial blue-shift ($\Delta\lambda \sim$ 55 nm) of the longitudinal plasmon resonance occurs upon transfer of Au nanorods from aqueous environment onto an ITO substrate. Predicted curves (dashed) based on results of COMSOL simulations and the dimensional analysis from TEM/SEM data (see Fig. 1) are also shown.

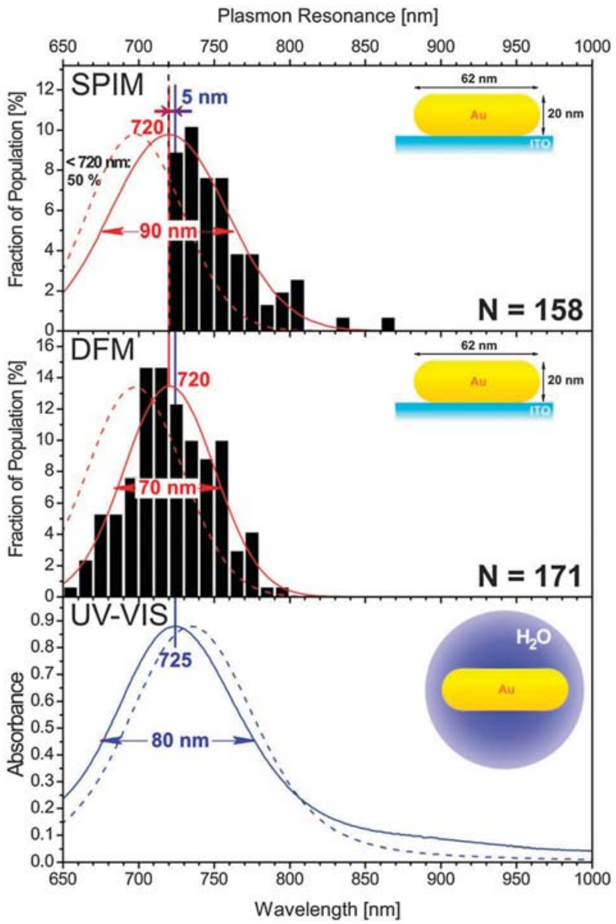

Fig. 8 Plasmon resonance distribution for Au nanorods [Sample 2: $\langle l \rangle$ = 63(5) nm, $\langle w \rangle$ = 20(2) nm] on ITO measured in SPIM (top) and DFM (middle) overlayed with the Gaussian best fits (solid lines). The missing fraction to the blue of our laser tuning range is inferred from SEM images. Minimal differences between the DFM and SPIM measurements are observed, consistent with observation that both techniques infer the same resonances. UV-VIS spectrum (solid line) of the aqueous solution of the same Au nanorods in bulk (bottom). Transfer of Au nanorods from water onto an ITO substrate induces a minimal blue-shift ($\Delta\lambda \sim$ 5 nm) in the longitudinal plasmon resonance. Predicted curves (dashed) based on results of COMSOL simulations and the TEM/SEM dimensional analysis of Sample 2 (see Fig. 1) are also shown.

where $d\lambda_{Pl}/dAR$ is obtained from the COMSOL calculated dependence of the plasmon resonance position on the rod aspect ratio, $\lambda_{Pl}(AR)$. Multiplication of $P(\lambda_{Pl})$ from eqn (3) with a bin size $\Delta\lambda_{Pl}$ = 10 nm yields predictions for the SPIM/DFM inferred population distributions (dashed lines in Fig. 7 and 8). To facilitate comparison between predicted and measured resonance peak positions/widths, the calculated distributions have been normalized to the peak value of the experimental fits.

To simulate the UV-VIS absorbance spectrum $A_{EXT}(\lambda)$, the calculated extinction cross-section spectra for each Au nanorod of different AR, $\sigma_{EXT}(\lambda, AR)$, must be integrated over the distribution of rod aspect ratios:

$$A_{EXT}(\lambda) \propto \int_0^\infty P(AR)\sigma_{EXT}(\lambda, AR)dAR \tag{4}$$

The resulting spectrum is normalized to the experimentally observed peak value and represented by dashed lines in Fig. 7. The predicted ensemble-averaged peak values for Au nanorods on ITO and in water are $\langle\lambda_{Pl}\rangle_L^{ITO} = 760$ nm and $\langle\lambda_{Pl}\rangle_L^{H_2O} = 807$ nm, respectively, *i.e.*, in excellent quantitive agreement with the experimentally inferred values of 765(5) nm and 820(2) nm. By way of futher confirmation, the peak width $[\sigma_L^{H_2O} = 70(5)\ \text{nm}]$ predicted for nanorods in H_2O agrees quite well with the experimentally observed value $[\sigma_L^{H_2O} = 60(5)\ \text{nm}]$, suggesting that the P(AR) distributions in Fig. 1 are acceptably accurate. Furthermore, the distribution of peak resonances for rods on ITO-glass exhibits a width comparable to, albeit narrower, than the predictions based on the structural data $[\sigma_L^{ITO} = 40(5)\ \text{nm}\ vs.\ 60(5)\ \text{nm}]$. Given the limited laser tuning range, this level of agreement seems entirely reasonable.

The corresponding population analysis of the longitudinal SPR distributions for the larger rods (Sample 2) is shown in Fig. 8. Due to Ti:Sapphire laser tuning range, the statistics indicate that only half of the true plasmon resonance peaks are observed. By way of compensation, however, these larger rods have ~6-fold larger volumes and consequently exhibit nominally 36-fold stronger scattering intensities, thus permitting the distribution inferred from SPIM [Fig. 8 (top)] to be supplemented with DFM measurements [Fig. 8 (middle)]. Interestingly, the ensemble-averaged plasmon resonance value for rods on

This journal is © the Owner Societies 2013

Published on 31 January 2013. Downloaded by University of Colorado at Boulder on 10/01/2014 19:38:12.

ITO, $\langle\lambda_{\mathrm{Pl}}\rangle_{\mathrm{L}}^{\mathrm{ITO}} = 720(2)$ nm, is nearly identical to the value for rods in an aqueous environment, $\langle\lambda_{\mathrm{Pl}}\rangle_{\mathrm{L}}^{\mathrm{H_2O}} = 725(2)$ nm, determined from the UV-VIS spectrum of a water solution of the same Au nanorod sample [Fig. 8 (bottom)]. The much smaller blue-shift [$\sim$5(5) nm] in the longitudinal SPR upon transfer of larger rods from water onto an ITO substrate contrasts the behavior observed in smaller rods. While numerical simulations predict an ensemble-average value for larger rods in water of $\langle\lambda_{\mathrm{Pl}}\rangle_{\mathrm{L}}^{\mathrm{H_2O}} = 734$ nm, in reasonable agreement with observations, the simulations also predict a $\langle\lambda_{\mathrm{Pl}}\rangle_{\mathrm{L}}^{\mathrm{ITO}} = 698$ nm for these rods on ITO, thus implying a 36 nm blue-shift. Consequently, the blue-shift in the longitudinal SPR upon rod transfer from an aqueous environment (n_w = 1.33) onto an ITO coated coverslip [n_{eff} = 1.25(5)] is experimentally observed and agrees reasonably well with numerical simulations.

IV. Discussion

Understanding the local dielectric environment and particle shape is critical for accurate modelling of the particle plasmonic response. Given this information, however, classical electrodynamics is sufficient for accurate predictions of particle's optical properties, as indicated by near quantitative agreement ($\pm$0.04 eV) between experiment and theory observed in the present work. The good agreement thus suggests that the experimental environment is reasonably accurately described by the assumptions employed in the numerical simulations. Specifically, the data are consistent with all materials (ITO, glass and Au) possessing bulk dielectric properties (with film refractive index well determined by ellipsometry), with rods parallel to the $\sim$20 nm thick ITO film, and little ligand coverage remaining on the rod surface.

This last point is noteworthy given the affinity of the CTAB molecules for the Au surface that keeps Au rods stable almost indefinitely in aqueous solutions and is thus expected to remain on the particle surface even after deposition. Even just a monolayer thick coating of these molecules ($\sim$2 nm) would significantly alter the effective dielectric constant of the rod environment and thus strongly shift the longitudinal SPR. The ability to accurately model the longitudinal plasmon resonance without the ligand implies the absence of such a layer. However, given that each pulse is estimated to heat the rods by up to $\sim$100–200 °C,[66] noncovalently bound molecules could be removed under vacuum conditions. Furthermore, the relatively low kinetic energy ($<$1.5 eV) electrons generated are expected to induce fragmentation of organic molecules and thus can also degrade the ligand layer.[81] However, the absence of any significant shifts in the longitudinal SPR between DFM measurements before and after SPIM investigation would also be consistent simply with ligand removal during sample preparation.

A potentially more important environmental factor affecting nanoparticle plasmon resonance dynamics is the ITO film. For example, surface adlayer on the substrate or variations in the substrate refractive index with depth or position on the surface could all significantly affect the particle plasmonic response.[68] However, the good agreement between experiment and calculation suggests that these contributions have been effectively incorporated into the measured refractive index of the ITO film. Indeed, ellipsometric determination of the dielectric properties of the ITO film and its thickness are found to be critical for attaining quantitative correspondence between theory and experiment.

Since the plasmon is affected by the dielectric environment extending only a short distance from the particle surface, a second property of the ITO film that can strongly influence the paticle plasmonic response is the film thickness (d_{f}). The characteristic depth ''sensed'' by the plasmon can be deduced from the plasmon-induced distribution of local electric fields surrounding the nanoparticle. For example, a cross-sectional view of the electric near-field enhancement for a l = 80 nm × w = 20 nm Au nanorod on a d_{f} = 18 nm ITO substrate is shown in Fig. 9(a). The plot reveals a rapidly decaying electric field enhancement with increasing distance from the rod, suggesting that the plasmon in large nanorods will be largely *insensitive* to substrate identity past $\sim$20 nm.

More quantitatively, the plasmon spatial extent can be deduced from lineouts through the electric field enhancement

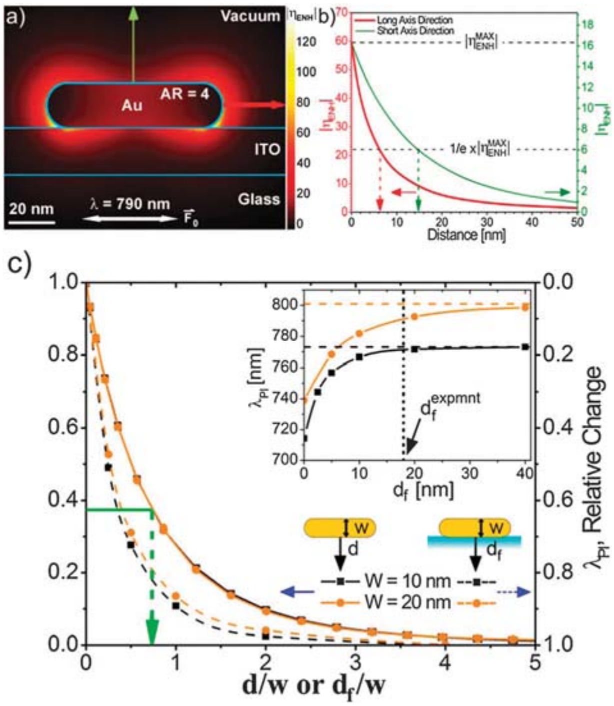

Fig. 9 (a) Map of electric near-field enhancement factor, $|\eta_{\mathrm{ENH}}|$, for a resonantly excited ($\lambda = \lambda_{\mathrm{Pl}}$ = 790 nm) Au nanorod (l = 80 nm; w = 20 nm) on d_{f} = 18 nm thick ITO film deposited on top of an infinite glass slab. (b) Lineouts in the major (thick solid) and minor (thin solid) rod axis directions. (c) (solid lines) Relative change in $|\eta_{\mathrm{ENH}}|$ *vs.* reduced distance d/w from the rod surface in the transverse direction, compared with (dashed lines) shift in LSPR λ_{Pl} as a function of reduced ITO film thickness (d_{f}/w) for w = 10 nm (squares) and w = 20 nm (circles) rods. The 1/e distance measures the spatial extent of the longitudinal plasmon in the transverse direction, as indicated by the arrow at d/w $\sim$ 0.75. Inset: LSPR λ_{Pl} as a function of ITO film thickness d_{f} for w = 10 nm (squares) and w = 20 nm (circles) rods together with the asymptotic value for an infinitely thick ITO slab (dashed). Dotted line marks the experimentally measured ITO film thickness.

Published on 31 January 2013. Downloaded by University of Colorado at Boulder on 10/01/2014 19:38:12.

map [Fig. 9(a)] in the direction of the major (longitudinal) and minor (transverse) rod axes shown in Fig. 9(b). In the transverse direction relevant to the present discussion, the 1/*e* distance is $\sim$15 nm and thus comparable to the film thickness, suggesting that an infinitely thick ITO slab should not be assumed for the substrate. Furthermore, these calculations indicate that this 1/*e* distance depends also on the particle size and grows approximately linearly with rod dimensions. For example, in Fig. 9(c) the plasmon field in the transverse direction is plotted as a function of reduced dimensions (relative to width *w*) for the two rod sizes. The overlap between the two is nearly exact in these reduced coordinates, implying that the plasmon extends approximately twice as far from the rod surface in case of larger (w = 20 nm) *vs.* smaller (w = 10 nm) rods, with a 1/*e* distance of approximately $\sim 0.7w$.

The effect of the ITO film thickness d_f on the longitudinal SPR peak wavelength is further quantitated in Fig. 9(c) (see inset) for the two studied rod sizes at AR = 4. A dramatic shift (60 nm) in the plasmon resonance is observed depending on whether the substrate is glass ($n \sim 1.5$) or ITO ($n \sim 2.0$). Furthermore, the smaller rods achieve the asymptotic value ($d_f \to \infty$), where the ITO film acts like bulk ITO, approximately twice as fast as the larger ones, in agreement with the above discussion that the plasmon spatially extends twice as far for larger *vs.* smaller rods. This is further confirmed by nearly overlapping datapoints in Fig. 9(c), where the normalized plasmon resonance shift is plotted as a function of film thickness in reduced coordinates (*i.e.*, d_f/w). This plot also reveals that the asymptotic limit can be assumed when film thickness exceeds $\sim 2w$, with negligible effect on the calculated longitudinal SPR position (±5% of the overall change). For the present samples, the d_f = 18 nm thick ITO film acts effectively as an infinite slab for the smaller rods (w = 10 nm), whereas the finite film thickness needs to be considered for accurate predictions in larger rods (w = 20 nm).

With a first principles understanding of the dominant factors that influence plasmonic behavior in supported Au NRs, we next compare the experimental sensitivities of the LSPR on rod aspect ratio with predictions of other models. We start off with a simple electrostatic description, where for a prolate ellipsoid made of a metal well-described by the Drude model, the following expression for the longitudinal SPR sensitivity on AR approximately holds at moderate AR values ($3 < \mathrm{AR} < 10$):[44]

$$\frac{\mathrm{d}\lambda_{\max}}{\mathrm{dAR}} = \frac{\kappa}{\omega_{\mathrm{Pl}} f(\mathrm{AR})} n_{\mathrm{m}} \tag{5}$$

In eqn (5), κ = 1239.85 nm eV, ω_{Pl} is the Drude metal plasma frequency [$\hbar\omega_{\mathrm{Pl}}$(Au) = 9.0 eV],[82] n_{m} the refractive index of the surrounding medium, and $f(\mathrm{AR}) \sim \sqrt{\ln(2\mathrm{AR}) - 1}$ is a slowly varying function of AR. The experimentally observed linear dependence of the longitudinal SPR on AR is correctly reproduced by the electrostatic model; however it predicts a sensitivity $\frac{\mathrm{d}\lambda_{\max}}{\mathrm{dAR}} = +162(7)$ nm if the experimentally determined effective refractive index is used for the Glass–ITO–Air interface, *i.e.*, $n_{\mathrm{m}} = n_{\mathrm{eff}}$ = 1.25(5) (see Fig. 6). This sensitivity is substantially larger than found both experimentally $\left[\frac{\mathrm{d}\lambda_{\max}}{\mathrm{dAR}} = +100(10)\ \mathrm{nm}\right]$ and theoretically ($\frac{\mathrm{d}\lambda_{\max}}{\mathrm{dAR}} = +104$ nm and $\frac{\mathrm{d}\lambda_{\max}}{\mathrm{dAR}} = +113$ nm for w = 10 nm and w = 20 nm rods, respectively), indicating the electrostatic approximation to be inadequate for a precise description of even small Au NRs. The model overestimates the dependence of longitudinal SPR on rod aspect ratio, with the discrepancy likely arising from an assumed ellipsoidal shape for nanoparticles.

A more comprehensive, empirical model has recently been proposed by Encina and Coronado for predicting longitudinal SPR of cylindrical rods in a uniform medium with a dielectric constant, ε_{m}:[42]

$$\lambda_{\max}[\mu\mathrm{m}] = \frac{\sqrt{\alpha_{\mathrm{D}} + \varepsilon_{\mathrm{m}}\left(\frac{\mathrm{AR}^2}{{l_{\mathrm{m}}}^2\pi^2}(Aw^2 + B) + C\right)}}{\beta_{\mathrm{D}}} \tag{6}$$

where A (2687 μm^{-2}), B (4.4) and C (3.7) are empirical constants derived from extensive series of DDA calculations, l_{m} is the plasmon mode order (*i.e.*, l_{m} = 1 for the dipolar, longitudinal SPR studied here) and α_{D} and β_{D} are constants in the Drude–Sommerfeld expression for the real part of the material dielectric function: $\varepsilon = \alpha_{\mathrm{D}} - {\beta_{\mathrm{D}}}^2\lambda^2$ (for Au, α_{D} = 9.84 and β_{D} = 7.3 μm^{-1}).[42] While a uniform surrounding medium has been assumed in the original derivation, the equation has recently also been applied to rods on a substrate, where an effective refractive index n_{eff} has been used instead.[44] The formula predicts a nearly linear dependence of the longitudinal SPR on AR (as well as n_{m}) for Au cylinders with AR > $\sim$4. For example, at AR = 4 and n_{eff} = 1.25 eqn (6) yields a sensitivity $\frac{\mathrm{d}\lambda_{\max}}{\mathrm{dAR}} \sim +80$ nm, thus slightly underestimating the actual value and underlining that the assumed rod shape strongly influences the predicted longitudinal plasmon behavior.

The model by Encina and Coronado is also one of the few models that attempts to explicitly include the overall rod size (*i.e.*, width) into the expression for the longitudinal SPR. The predicted LSPR as a function of rod width w is plotted in Fig. 5 (dashed line), based on the empirically determined effective refractive index n_{eff} = 1.25. While the model nicely reproduces the parabolic dependence calculated in the present work for Au lozenges (solid line), the red-shift increases more rapidly with rod width w than predicted by our model. The reason for this is that we have assumed a constant ITO film thickness of d_f = 18 nm, whereas there is an additional depth sensitivity for wider rods to the underlying low index glass layer, thus resulting in a progressively smaller effective refractive index for the surrounding medium n_{m}. In addition, eqn (6) predicts longitudinal SPR values *blue-shifted* by $\sim$50 nm compared to observations, again highlighting the fact that chemically synthesized Au nanorods can not be assumed to behave either like ellipsoids or cylinders and that detailed numerical calculations on the exact particle shape are critical for accurate determination of their plasmonic response.

Published on 31 January 2013. Downloaded by University of Colorado at Boulder on 10/01/2014 19:38:12.

Lastly, we explore the concept of an "effective refractive index" n_{eff} or dielectric constant often introduced [as in eqn (1)] to model the asymmetric environment of particles on a substrate. Though clearly approximate, this can be quite useful in allowing analytical theories generally derived for particles in uniform media to be applied even in the case of more complicated environments.[58–61] This effective index n_{eff} requires *a priori* knowledge of the weighting factor α, which quantifies the particle sensitivity to the superstrate and substrate. For example, this work has experimentally determined $\alpha = 0.75(5)$ for lozenge-shaped nanoparticles, thus implying the dielectric sensitivity of the rod plasmonic response on the substrate only at the $1 - \alpha \cong 25(5)\%$ level.

However, there are also more *ad hoc* theoretical approaches for estimating α that do not require detailed electrodynamics calculations.[61] In the simpler "geometrical" method, a sensing shell of some thickness (typically, the $1/e$ distance for the electric field enhancement) surrounding the particle is divided into a volume that lies in the substrate, V_{sub}, and a volume that lies in the superstrate, V_{super}. The weighting factor α is then simply calculated using:

$$\alpha \approx \frac{V_{\text{super}}}{V_{\text{super}} + V_{\text{sub}}}. \tag{7}$$

In a more complicated, but also physically better motivated approach, the substrate and superstrate volume elements are first weighted by an exponentially decreasing function of distance from the particle surface that models a typical distance dependence of a plasmonic field. To calculate α, an equation analogous to (7) is then applied.[61] As a simple test, we have used both methods to calculate α in the case of hemispherically capped cylinders (*i.e.*, lozenges) in direct contact with the substrate (see Appendix). For rods with AR = 4, the geometric approach results in a weighting parameter of $\alpha \approx 0.70$, whereas the more physically motivated model yields $\alpha \approx 0.61$. Note that both these values underestimate the experimentally determined value of $\alpha = 0.75(5)$, with the simpler geometric approach faring better than the plasmonically weighted method. For example, the former approach predicts a plasmon resonance centered at $\lambda_{\text{Pl}} \sim 800$ nm to be *red*-shifted by ~ 20 nm, whereas ~ 60 nm red-shift is predicted by the latter method. Nevertheless, given the simplicity of these approaches, the α values still should be useful for prediction of plasmon resonances at the semiquantitative (±0.1 eV) level.

V. Conclusions

Longitudinal plasmon resonances in Au nanorods on ITO have been studied (i) experimentally *via* multiphoton photoelectron emission in a scanning photoionization microscope (SPIM) and (ii) theoretically with a finite element analysis as implemented in COMSOL. Since the observed photoemission resonances in Au nanorods directly reflect the rod scattering resonances, the SPIM studies complement dark-field microscopy by allowing smaller particles to be studied. Experimentally determined longitudinal plasmon resonances are found to be in very good agreement with numerical predictions, indicating that classical electrodynamics based on a bulk dielectric function of the materials involved describes plasmonic response reasonably well. However, ellipsometric characterization of the dielectric properties and thickness of the ITO film is critical for achieving this degree of nearly quantitative agreement with the experiment. The film thickness has been shown to be an important parameter for values smaller than twice the rod width, *i.e.*, $d_{\text{f}} < 2w$. The sensitivity of the longitudinal SPR in chemically synthesized rods on their aspect ratio and dielectric environment has also been quantified to be $\frac{\mathrm{d}\lambda_{\max}}{\mathrm{dAR}} = +100(10)$ nm and $\frac{\mathrm{d}\lambda_{\max}}{\mathrm{d}n_{\text{m}}} \sim +450$ nm, respectively. We furthermore demonstrate that for most accurate predictions (±0.04 eV; *i.e.*, ±20 nm at 800 nm), calculations in the electrostatic limit can not be used to predict the plasmonic response of rods for $l > 50$ nm or $w > 15$ nm. For a typical shape of the chemically synthesized rods (*i.e.*, hemispherically capped cylinders – lozenges), the sensitivity to the substrate has been measured in terms of a weighting factor $\alpha \approx 0.75(5)$ [see eqn (1)], suggesting that the substrate contributes only $1 - \alpha \approx 0.25(5)$ to the overall dielectric effects. Consequently, in spite of the rather large refractive index of ITO in the wavelengh range studied ($n \sim 2.0$), only a small blueshift (~5–50 nm) is experimentally observed when Au nanorods are transferred from an aqueous solution ($n \sim 1.33$) onto an ITO-coated glass coverslip. Overall, the study highlights the importance of detailed numerical calculations for predictions of the plasmonic response for supported nanoparticles as well as provides essential experimental benchmarks for nanorod geometries on ITO substrates of interest in a wide variety of applications.

Appendix

To calculate the weighting factor α, and thus model asymmetric surroundings in terms of a uniform environment with an effective refractive index given by eqn (1), Curry *et al.* outlined two methods mirrored in the present derivation for the lozenge shape.[61] In the geometric approach, the following expression is obtained if the sensing volume extends a rod width (w) distance from the rod surface:

$$\alpha = \frac{38\pi + 3(\mathrm{AR} - 1)\left(7\pi/2 + 2\sqrt{2} + 9\arcsin(1/3)\right)}{52\pi + 24\pi(\mathrm{AR} - 1)} \tag{A.1}$$

In the physically motivated (plasmonically weighted) model, the lozenge is divided into a central, cylindrical part and the two spherical end-caps. This allows the two required volume integrals for calculating α to be obtained from contributions (i) of the two end-caps based on a derivation for a sphere [yields $I_1 = 2\pi r_0^{\,2}(2r_0 + w/2)$ and $I_2 = 2\pi r_0 w(r_0 + w/2)$],[61] and (ii) of the cylindrical section for which the following two integrals need to be numerically calculated:

$$I_3 = w(\mathrm{AR} - 1)\int_{w/2}^{\infty}\int_{0}^{\infty} \mathrm{e}^{-\frac{\sqrt{\rho^2 + z^2} - w/2}{r_0}}\,\mathrm{d}\rho\,\mathrm{d}z \tag{A.2}$$

$$I_4 = w(\mathrm{AR} - 1)\int_{-w/2}^{w/2}\int_{\sqrt{\frac{w^2}{4} - z^2}}^{\infty} \mathrm{e}^{-\frac{\sqrt{\rho^2 + z^2} - w/2}{r_0}}\,\mathrm{d}\rho\,\mathrm{d}z \tag{A.3}$$

Published on 31 January 2013. Downloaded by University of Colorado at Boulder on 10/01/2014 19:38:12.

From these four integrals, the weighting factor can be calculated:

$$\alpha = \frac{I_1 + I_2 + I_3 + I_4}{2I_1 + I_2 + 2I_3 + I_4} \quad \text{(A.4)}$$

and for $r_0 = w$ results in the following numerically approximate expression (see Fig. 9):

$$\alpha \cong \frac{8\pi + 3.95(\mathrm{AR} - 1)}{13\pi + 5.78(\mathrm{AR} - 1)} \quad \text{(A.5)}$$

Acknowledgements

This work has been supported by the Air Force Office of Scientific Research (FA9550-12-1-0139), with additional funds for optics, microscopy and computer resources provided by the National Science Foundation (CHE1012685, PHYS1125844) and the National Institute for Standards and Technology. We would also like to thank Dave Alchenberger for help with SEM instrumentation and ellipsometry measurements.

References

1 G. Mie, *Ann. Phys.*, 1908, **25**, 377–445.
2 H. A. Atwater and A. Polman, *Nat. Mater.*, 2010, **9**, 205–213.
3 S. Pillai, K. R. Catchpole, T. Trupke and M. A. Green, *J. Appl. Phys.*, 2007, **101**, 093105.
4 D. M. Schaadt, B. Feng and E. T. Yu, *Appl. Phys. Lett.*, 2005, **86**, 063106.
5 H. R. Stuart and D. G. Hall, *Appl. Phys. Lett.*, 1996, **69**, 2327–2329.
6 W. L. Barnes, A. Dereux and T. W. Ebbesen, *Nature*, 2003, **424**, 824–830.
7 E. Ozbay, *Science*, 2006, **311**, 189–193.
8 J. A. Schuller, E. S. Barnard, W. S. Cai, Y. C. Jun, J. S. White and M. L. Brongersma, *Nat. Mater.*, 2010, **9**, 193–204.
9 G. Baffou, R. Quidant and F. J. G. de Abajo, *ACS Nano*, 2010, **4**, 709–716.
10 I. H. El-Sayed, X. H. Huang and M. A. El-Sayed, *Nano Lett.*, 2005, **5**, 829–834.
11 N. L. Rosi and C. A. Mirkin, *Chem. Rev.*, 2005, **105**, 1547–1562.
12 P. Alivisatos, *Nat. Biotechnol.*, 2004, **22**, 47–52.
13 J. N. Anker, W. P. Hall, O. Lyandres, N. C. Shah, J. Zhao and R. P. Van Duyne, *Nat. Mater.*, 2008, **7**, 442–453.
14 J. P. Camden, J. A. Dieringer, Y. M. Wang, D. J. Masiello, L. D. Marks, G. C. Schatz and R. P. Van Duyne, *J. Am. Chem. Soc.*, 2008, **130**, 12616–12617.
15 A. M. Michaels, M. Nirmal and L. E. Brus, *J. Am. Chem. Soc.*, 1999, **121**, 9932–9939.
16 S. M. Nie and S. R. Emery, *Science*, 1997, **275**, 1102–1106.
17 K. A. Stoerzinger, J. Y. Lin and T. W. Odom, *Chem. Sci.*, 2011, **2**, 1435–1439.
18 C. E. Talley, J. B. Jackson, C. Oubre, N. K. Grady, C. W. Hollars, S. M. Lane, T. R. Huser, P. Nordlander and N. J. Halas, *Nano Lett.*, 2005, **5**, 1569–1574.
19 K. A. Willets and R. P. Van Duyne, in *Annual Review of Physical Chemistry, Annual Reviews*, Palo Alto, 2007, vol. 58, pp. 267–297.
20 D. K. Polyushkin, E. Hendry, E. K. Stone and W. L. Barnes, *Nano Lett.*, 2011, **11**, 4718–4724.
21 J. C. Hulteen, D. A. Treichel, M. T. Smith, M. L. Duval, T. R. Jensen and R. P. Van Duyne, *J. Phys. Chem. B*, 1999, **103**, 3854–3863.
22 B. Nikoobakht and M. A. El-Sayed, *Chem. Mater.*, 2003, **15**, 1957–1962.
23 S. J. Oldenburg, J. B. Jackson, S. L. Westcott and N. J. Halas, *Appl. Phys. Lett.*, 1999, **75**, 2897–2899.
24 A. Sanchez-Iglesias, I. Pastoriza-Santos, J. Perez-Juste, B. Rodriguez-Gonzalez, F. J. G. de Abajo and L. M. Liz-Marzan, *Adv. Mater.*, 2006, **18**, 2529–2534.
25 Y. G. Sun and Y. N. Xia, *Science*, 2002, **298**, 2176–2179.
26 J. Turkevich, P. C. Stevenson and J. Hillier, *Discuss. Faraday Soc.*, 1951, **11**, 55–75.
27 R. C. Jin, Y. W. Cao, C. A. Mirkin, K. L. Kelly, G. C. Schatz and J. G. Zheng, *Science*, 2001, **294**, 1901–1903.
28 J. Y. Chen, B. Wiley, Z. Y. Li, D. Campbell, F. Saeki, H. Cang, L. Au, J. Lee, X. D. Li and Y. N. Xia, *Adv. Mater.*, 2005, **17**, 2255–2261.
29 N. R. Jana, L. Gearheart and C. J. Murphy, *J. Phys. Chem. B*, 2001, **105**, 4065–4067.
30 B. J. Wiley, Y. J. Xiong, Z. Y. Li, Y. D. Yin and Y. N. Xia, *Nano Lett.*, 2006, **6**, 765–768.
31 J. Zhang, S. Z. Li, J. S. Wu, G. C. Schatz and C. A. Mirkin, *Angew. Chem., Int. Ed.*, 2009, **48**, 7787–7791.
32 C. J. Murphy, T. K. San, A. M. Gole, C. J. Orendorff, J. X. Gao, L. Gou, S. E. Hunyadi and T. Li, *J. Phys. Chem. B*, 2005, **109**, 13857–13870.
33 A. V. Alekseeva, V. A. Bogatyrev, B. N. Khlebtsov, A. G. Mel'nikov, L. A. Dykman and N. G. Khlebtsov, *Colloid J.*, 2006, **68**, 661–678.
34 S. S. Chang, C. W. Shih, C. D. Chen, W. C. Lai and C. R. C. Wang, *Langmuir*, 1999, **15**, 701–709.
35 R. Gans, *Ann. Phys.*, 1912, **37**, 881–900.
36 B. M. I. van der Zande, M. R. Bohmer, L. G. J. Fokkink and C. Schonenberger, *J. Phys. Chem. B*, 1997, **101**, 852–854.
37 Y. Y. Yu, S. S. Chang, C. L. Lee and C. R. C. Wang, *J. Phys. Chem. B*, 1997, **101**, 6661–6664.
38 S. Link, M. B. Mohamed and M. A. El-Sayed, *J. Phys. Chem. B*, 1999, **103**, 3073–3077.
39 C. Novo, D. Gomez, J. Perez-Juste, Z. Y. Zhang, H. Petrova, M. Reismann, P. Mulvaney and G. V. Hartland, *Phys. Chem. Chem. Phys.*, 2006, **8**, 3540–3546.
40 J. Perez-Juste, I. Pastoriza-Santos, L. M. Liz-Marzan and P. Mulvaney, *Coord. Chem. Rev.*, 2005, **249**, 1870–1901.
41 S. Link and M. A. El-Sayed, *J. Phys. Chem. B*, 1999, **103**, 8410–8426.
42 E. R. Encina and E. A. Coronado, *J. Phys. Chem. C*, 2007, **111**, 16796–16801.
43 A. L. Schmucker, N. Harris, M. J. Banholzer, M. G. Blaber, K. D. Osberg, G. C. Schatz and C. A. Mirkin, *ACS Nano*, 2010, **4**, 5453–5463.

This journal is © the Owner Societies 2013

Published on 31 January 2013. Downloaded by University of Colorado at Boulder on 10/01/2014 19:38:12.

44 L. S. Slaughter, W. S. Chang, P. Swanglap, A. Tcherniak, B. P. Khanal, E. R. Zubarev and S. Link, *J. Phys. Chem. C*, 2010, **114**, 4934–4938.

45 S. W. Prescott and P. Mulvaney, *J. Appl. Phys.*, 2006, **99**, 123504.

46 G. W. Bryant, F. J. G. De Abajo and J. Aizpurua, *Nano Lett.*, 2008, **8**, 631–636.

47 B. N. Khlebtsov and N. G. Khlebtsov, *J. Phys. Chem. C*, 2007, **111**, 11516–11527.

48 M. M. Miller and A. A. Lazarides, *J. Phys. Chem. B*, 2005, **109**, 21556–21565.

49 A. C. Templeton, J. J. Pietron, R. W. Murray and P. Mulvaney, *J. Phys. Chem. B*, 2000, **104**, 564–570.

50 S. Underwood and P. Mulvaney, *Langmuir*, 1994, **10**, 3427–3430.

51 H. J. Chen, X. S. Kou, Z. Yang, W. H. Ni and J. F. Wang, *Langmuir*, 2008, **24**, 5233–5237.

52 K. C. Vernon, A. M. Funston, C. Novo, D. E. Gomez, P. Mulvaney and T. J. Davis, *Nano Lett.*, 2010, **10**, 2080–2086.

53 C. Novo, A. M. Funston, I. Pastoriza-Santos, L. M. Liz-Marzan and P. Mulvaney, *J. Phys. Chem. C*, 2008, **112**, 3–7.

54 H. J. Chen, T. Ming, S. R. Zhang, Z. Jin, B. C. Yang and J. F. Wang, *ACS Nano*, 2011, **5**, 4865–4877.

55 R. Ruppin, *Surf. Sci.*, 1983, **127**, 108–118.

56 R. Ruppin, *Physica A*, 1991, **178**, 195–205.

57 P. A. Bobbert and J. Vlieger, *Physica A*, 1987, **147**, 115–141.

58 H. Tamaru, H. Kuwata, H. T. Miyazaki and K. Miyano, *Appl. Phys. Lett.*, 2002, **80**, 1826–1828.

59 A. Hilger, M. Tenfelde and U. Kreibig, *Appl. Phys. B: Lasers Opt.*, 2001, **73**, 361–372.

60 C. Sonnichsen, S. Geier, N. E. Hecker, G. von Plessen, J. Feldmann, H. Ditlbacher, B. Lamprecht, J. R. Krenn, F. R. Aussenegg, V. Z. H. Chan, J. P. Spatz and M. Moller, *Appl. Phys. Lett.*, 2000, **77**, 2949–2951.

61 A. Curry, G. Nusz, A. Chilkoti and A. Wax, *Opt. Express*, 2005, **13**, 2668–2677.

62 J. Zuloaga and P. Nordlander, *Nano Lett.*, 2011, **11**, 1280–1283.

63 B. M. Ross and L. P. Lee, *Opt. Lett.*, 2009, **34**, 896–898.

64 B. J. Messinger, K. U. Vonraben, R. K. Chang and P. W. Barber, *Phys. Rev. B: Condens. Matter Mater. Phys.*, 1981, **24**, 649–657.

65 N. K. Grady, N. J. Halas and P. Nordlander, *Chem. Phys. Lett.*, 2004, **399**, 167–171.

66 A. Grubisic, V. Schweikhard, T. A. Baker and D. J. Nesbitt, *ACS Nano*, 2013, **7**, 87–99.

67 B. Johs, J. A. Woollam, C. Herzinger, J. Hilfiker, R. Synowicki and C. Bungay, *SPIE Proceedings Series*, 1999, **CR72**, 29–58.

68 W. F. Wu and B. S. Chiou, *Appl. Surf. Sci.*, 1993, **68**, 497–504.

69 H. B. Michaelson, *J. Appl. Phys.*, 1977, **48**, 4729–4733.

70 R. Schlaf, H. Murata and Z. H. Kafafi, *J. Electron Spectrosc. Relat. Phenom.*, 2001, **120**, 149–154.

71 O. L. A. Monti, T. A. Baker and D. J. Nesbitt, *J. Chem. Phys.*, 2006, **125**, 154709.

72 V. Schweikhard, A. Grubisic, T. A. Baker and D. J. Nesbitt, *J. Phys. Chem. C*, 2011, **115**, 83–91.

73 L. Douillard, F. Charra, Z. Korczak, R. Bachelot, S. Kostcheev, G. Lerondel, P. M. Adam and P. Royer, *Nano Lett.*, 2008, **8**, 935–940.

74 V. Schweikhard, A. Grubisic, T. A. Baker, I. Thomann and D. J. Nesbitt, *ACS Nano*, 2011, **5**, 3724–3735.

75 A. I. Henry, J. M. Bingham, E. Ringe, L. D. Marks, G. C. Schatz and R. P. Van Duyne, *J. Phys. Chem. C*, 2011, **115**, 9291–9305.

76 P. B. Johnson and R. W. Christy, *Phys. Rev. B: Solid State*, 1972, **6**, 4370–4379.

77 F. A. Jenkins and H. E. White, *Fundamentals of Optics*, McGraw-Hill, Inc., New York, 4th edn, 1981.

78 V. Myroshnychenko, J. Rodriguez-Fernandez, I. Pastoriza-Santos, A. M. Funston, C. Novo, P. Mulvaney, L. M. Liz-Marzan and F. J. G. de Abajo, *Chem. Soc. Rev.*, 2008, **37**, 1792–1805.

79 Due to the limited laser tuning range, the values reflect a simple linear fit to Sample 2 data for AR > 3.2 nanorods, with the slope for Sample 1 data constrained to be the same.

80 W. Ni, X. Kou, Z. Yang and J. F. Wang, *ACS Nano*, 2008, **2**, 677–686.

81 L. Sanche, *Radical and Radical Ion Reactivity in Nucleic Acid Chemistry*, John Wiley & Sons, New York, 2009.

82 M. A. Ordal, R. J. Bell, R. W. Alexander, L. L. Long and M. R. Querry, *Appl. Opt.*, 1985, **24**, 4493–4499.